RESEARCH ARTICLE

Holographic optogenetic stimulation with calcium imaging as an all optical tool for cardiac electrophysiology

Sebastian Junge[1,2] | **Felix Schmieder**[3] ⓘ | **Philipp Sasse**[4] | **Jürgen Czarske**[3,5] |
Maria Leilani Torres-Mapa[1,2]* ⓘ | **Alexander Heisterkamp**[1,2]*

[1]Institute of Quantum Optics, Gottfried Wilhelm Leibniz University, Hannover, Germany

[2]Lower Saxony Centre for Biomedical Engineering, Implant Research and Development (NIFE), Hannover, Germany

[3]Faculty of Electrical and Computer Engineering, Laboratory of Measurement and Sensor System Technique and Competence Center Biomedical Computational Laser Systems (BIOLAS), TU Dresden, Dresden, Germany

[4]Medical Faculty, Institute of Physiology I, University of Bonn, Bonn, Germany

[5]Faculty of Physics, School of Science and Excellence Cluster Physics of Life, TU Dresden, Dresden, Germany

*Correspondence
Maria Leilani Torres-Mapa and Alexander Heisterkamp, Institute of Quantum Optics, Gottfried Wilhelm Leibniz University, Hannover, Germany.
Email: torres@iqo.uni-hannover.de and heisterkamp@iqo.uni-hannover.de

Abstract

All optical approaches to control and read out the electrical activity in a cardiac syncytium can improve our understanding of cardiac electrophysiology. Here, we demonstrate optogenetic stimulation of cardiomyocytes with high spatial precision using light foci generated with a ferroelectric spatial light modulator. Computer generated holograms binarized by bidirectional error diffusion create multiple foci
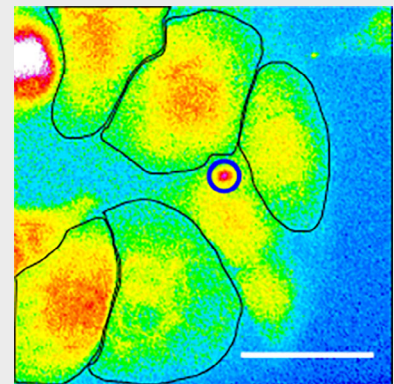
with more even intensity distribution compared with thresholding approach. We evoke the electrical activity of cardiac HL1 cells expressing the channelrhodopsin-2 variant, ChR2(H134R) using single and multiple light foci and at the same time visualize the action potential using a calcium sensitive indicator called Cal-630. We show that localized regions in the cardiac monolayer can be stimulated enabling us to initiate signal propagation from a precise location. Furthermore, we demonstrate that probing the cardiac cells with multiple light foci enhances the excitability of the cardiac network. This approach opens new applications in manipulating and visualizing the electrical activity in a cardiac syncytium.

KEYWORDS
calcium imaging, cardiac electrophysiology, channelrhodopsin, optogenetics, spatial light modulator, wavefront shaping

1 | INTRODUCTION

Optogenetics offers possibilities for treating cardiac arrhythmia and investigate the mechanisms of cardiac electrophysiology. At present, electrical stimulation is still the gold standard in probing and therapeutic treatment of cardiac diseases [1,2]. For example, cardiac pacemakers and cardioverter-defibrillators are considered safe and reliable medical devices implanted to millions of people worldwide [3,4]. However, with the advancement in tissue engineering and viral gene transfer, optogenetics creates potentially new routes for cardiac therapy [1,2].

Though at its infancy, optogenetics has shown great promise and has been applied to pace whole hearts in vivo [5,6] and resynchronize hearts after arrhythmia [7–9]. Analogous to electrical stimulation, optogenetics as a therapy requires fundamental studies to be performed on cellular, tissue level or animal models to understand how it can be effectively used to control cardiac systems. Particularly, the design of measurement protocols for cardiac electrophysiology could improve our understanding of the effectiveness and limitations of the technique. Therefore, along with the improvement of opsin variants and read-outs, developing optical technologies for spatially and temporally precise light delivery is also crucial.

The optical systems employed for optogenetic experiments would highly depend on the experimental design. For example, for the unspecific stimulation of a large mass of cells, hundreds of mm^2 in area, one could use incoherent light sources such as LEDs coupled to optical fibers or directed to the sample using free space optics [8,10,11]. However, for more intricate light stimulation to investigate cell to cell communication with single cell specificity, more advanced optical systems which can spatially confine light in subcellular dimensions are necessary. For example, stimulation of multiple cells in a network may either be performed by scanning the focused laser [12,13] or splitting the incident beam to multiple spots [14] to flexibly target any cells in a field of view while simultaneously observing the neuronal or cardiac network activity using fluorescence imaging. Galvanometer mirrors [12,15] or acousto-optical deflectors [16] which can be operated in kHz or MHz rate, respectively, can also be used to scan the laser spot in multiple positions within the cell or on multiples of cells. However, the photostimulation occurs sequentially and the temporal resolution will be limited by the dwell time necessary to optogenetically stimulate the individual cells [17].

For simultaneous parallel stimulation, the modulation of light's amplitude using digital mirror device (DMD) or both amplitude and phase using holographic methods via spatial light modulator (SLM) would therefore be desirable. A distinct advantage of phase and amplitude methods for optogenetic stimulation is the ability to shape the light arbitrarily and split the incident beam into multiple spots allowing simultaneous stimulation of multiples of cells. In cardiac networks, DMD devices have been mainly used especially for shaped light stimulation in mouse heart preparations and cardiac cell monolayers [18–20]. DMDs operate in a binary fashion wherein light is either deflected towards or away from the sample depending on the angular position of the micro mirrors. A disadvantage of DMD technology is its poor efficiency [21] which poses a problem for light sources with limited photon budget. SLMs on the other hand have been successfully implemented in neuroscience research especially for two-photon 3D parallel stimulation in the intact mouse brain. These devices are more photon efficient and have been effectively used in targeting cells in tissue slices and within the scattering brain environment [22–24]. Their slow response, typically at 60 Hz for liquid crystal technology can limit their applications when the pattern of light has to be updated in a fast manner. The trade-off between speed and photon efficiency leads to the use of ferroelectric SLMs with kHz frame rates. Ferroelectric SLMs (FSLMs) employ binary phase holograms which are considered more efficient for beam shaping compared with binary amplitude approaches [25]. In optogenetics field, FSLMs have been successfully employed to stimulate ChR2-expressing retinal ganglion cells [26] and induced pluripotent stem cells derived neurons [27].

In this study, we contribute to the optical toolbox for cell-specific and parallel optogenetic stimulation in cardiac cells. We demonstrate the use of a holographic FSLM system to deliver localized laser foci for optogenetic stimulation in a cardiomyocyte monolayer. An advantage of this setup is the delicate control of spatial location of excitability allowing single cell targeting of optogenetic cells. Using this system, parallel stimulation of multiple cells can be performed and electrical signaling can be redirected flexibly. To evaluate the excitability of the photostimulated cells, we used calcium imaging to detect the electrical activity in the immortalized cardiomyocyte cell line, HL1 cells. Furthermore, we investigate the effect of spatial summation of photocurrents using targeted dual spot stimulation. Overall, we present an all-optical tool for both localized and simultaneous excitation of multiple cells using a holographic approach as well as visualization of cardiac electrical activity with calcium imaging.

FIGURE 1 (A) Schematic diagram of the experimental setup with components specified. From top to bottom: SLM—spatial light modulator, L1–L4—lenses, $\frac{\lambda}{2}$—half wave plate, LP—linear polarizer, BS—beam splitter, DM—dichroic mirror, Exc—excitation filter, Em—emission filter, EMCCD—electron multiplying CCD camera. (B) Spectral properties of the components used in this experiment (from left to right), including the action spectra of ChR2 (H134R) data from [29], 488 nm laser, Cal-630 absorption and emission [30] and the filters used (Exc, Em and DM) [31]. (C) Confocal image of the HL1 cells expressing channelrhodopsin-2. Fluorescent signal shows the enhanced yellow fluorescent protein fused to ChR2 localized in the cell membrane. Scale bar is 200 μm
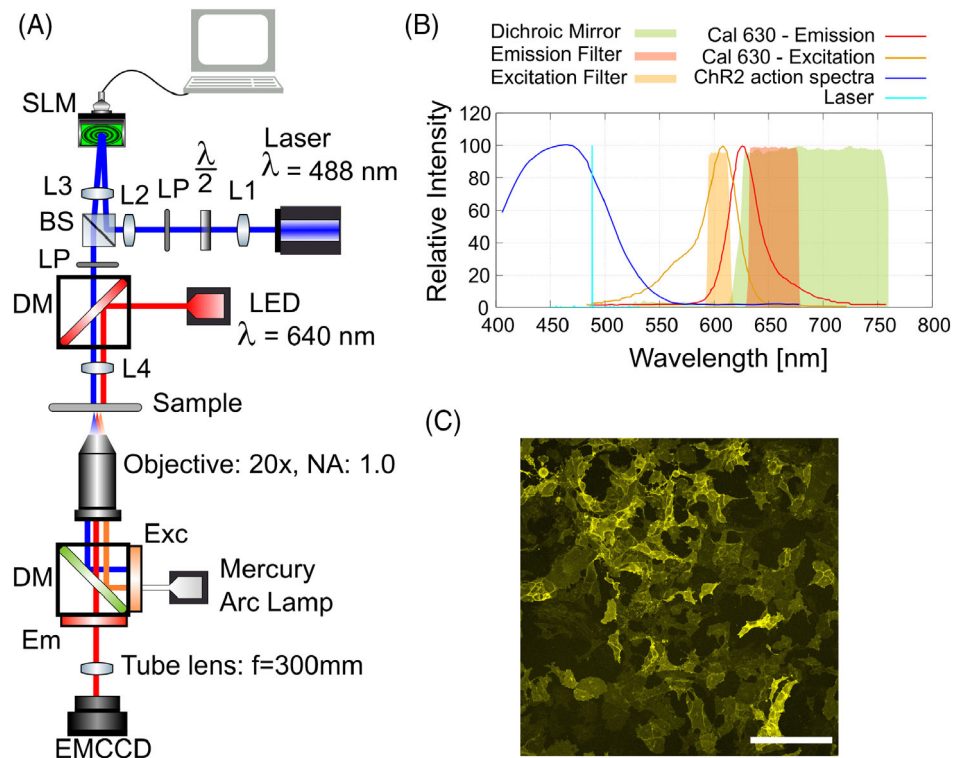
2 | MATERIALS AND METHODS

2.1 | Experimental setup

The schematic diagram of the experimental setup is shown in Figure 1A. A continuous wave laser with a wavelength of 488 nm (Coherent, Obis) is used to excite the ChR2-expressing cells. The beam is magnified by a Keplerian telescope (L1, L2) to illuminate the active area of a binary phase-only ferroelectric liquid crystal spatial light modulator (FSLM, M150 QXGA, Forth Dimension Displays) with a pixel pitch of 8.2 μm and 2048 × 1536 pixels. A half waveplate (λ/2) and a linear polarizer (LP) control the polarization of the incident light on the SLM. The zeroth order diffracted light reflected from the SLM, with its polarization rotated by $\pi/3$ is transmitted by a 50:50 beamsplitter (BS). A second polarizer ensures true 0-π phase modulation, transmitting polarization states with opposing sign. Lenses (L3 and L4) focus the zeroth diffraction order beam to a spot size of 3 μm at the sample plane. This approach compared with Fourier configuration, allows for a larger field of view while efficiently focusing the laser to illuminate the cells, albeit with a lower contrast due to undiffracted light. For brightfield imaging, a red LED (M660L4, Thorlabs) with a center wavelength of 640 nm was used to illuminate the sample. Computer generated binary holograms (CGH) derived from complex-valued Fresnel holograms and binarized

via bidirectional error diffusion [28] are displayed on the SLM to control the position and number of the laser foci used to excite the cells. Control of the SLM and CGH calculation are executed using a custom Matlab script. Lateral shifts of the hologram result in lateral shifts of the foci on the sample. The maximum frame rate of the SLM is 1.7 kHz for fast update of the CGH but was set to lower pre-set values to set the photostimulation duration (t_{pulse}) to 10 ms as performed in this study. CGH displayed on the SLM were updated as dictated by an external trigger. The photostimulation event and frequency are controlled by synchronizing CGH display to TTL signals from an external trigger which is synchronized with the start of the camera acquisition.

Figure 1B shows the combination of filters for calcium imaging along with the spectral properties of both the ChR2(H134R) and Cal-630. A home-built inverted microscope was used for calcium imaging. Fluorescence calcium imaging was performed using a mercury vapor short arc lamp (XCite 120PCQ, Excelitas) for fluorophore excitation. A high numerical aperture objective (Nikon, NA: 1.0) focuses the excitation light as well as collects the emitted light from the sample. A band-pass filter (Exc, Semrock, 605/15, FF01-605/15–25) centered at 605 nm selects a narrow spectral band (598–613 nm) of the arc lamp to excite Cal-630 which has a peak absorption at 605 nm. A dichroic mirror (DM, Semrock, 624, FF624-Di01-25×26×2.0) reflects the excitation light and

transmits the fluorescence signal. A long-pass filter (Em, Semrock, 655/40, FF02-655/40-25) ensures that only fluorescence is collected by the tube lens ($f = 300$ mm) which forms an image of the sample on an EMCCD camera (Andor iXon DU-885 K-CSO). Excitation light used for calcium imaging was measured using a photodiode power sensor (Thorlabs, S121C). Due to the slow calcium dynamics of HL1 cells, imaging was performed at relatively low frame rates, in our case, 11.6 frames/sec at full field of view (222.8 μm × 222.4 μm).

2.2 | Cell culture

For the experiments, we used a stably ChR2(H134R) expressing HL1 murine tumor cell line of atrial in origin which is known to maintain a cardiomyocyte-like phenotype. HL1 cells were generated by transduction with lentiviruses encoding for EF1α-ChR2(H134R)-EYFP to express ChR2(H134R) in fusion to the yellow fluorescent protein as reported earlier [32]. Cells were cultured in Claycomb media (Sigma-Aldrich) supplemented with 10% fetal bovine serum (Sigma-Aldrich), 1% L-glutamine (Sigma-Aldrich), 1% norepinephrine (Sigma-Aldrich) and 1% penicillin and streptomycin (Biochrom). The cell culture medium was changed every 24 h. Cells were kept at low passage numbers and passaged twice a week. HL1 cells (Sigma-Aldrich) that were not transduced with ChR2 were also cultured similarly and used as control.

2.3 | Sample preparation

Cells were seeded in a 35 mm glass bottom dish, previously coated with fibronectin (5 mg/L, Sigma-Aldrich) in 0.02% gelatine (Sigma-Aldrich). Approximately, 100 000 cells were seeded per dish and incubated for 24 to 48 h before experiments. To stain the cells with the calcium sensitive fluorophore, cells were washed with Dulbecco phosphate buffer solution (DPBS) without Ca^{2+} and Mg^{2+} (PanBiotech). 500 μL of HL1 culture medium containing Cal-630 (Biochrom) in dimethyl sulfoxide (Sigma Aldrich) with a final dye concentration of 20 μM were added to the dish. Dishes were incubated for 45 min at 37 °C. Afterwards, the medium of the dishes was changed to a fresh complete medium and the cells were incubated for further 30 min at 37 °C for deesterification.

2.4 | Spot characterization

To characterize the foci created by the FSLM, a series of computer generated holograms corresponding to 1 to 16 foci was calculated and subsequently uploaded to the FSLM. The images of the laser foci were captured using Andor Solis software with laser settings and the exposure time fixed for all images. Dark images were also taken with the same camera acquisition settings but without the laser foci. The intensity and profile of each spot was analyzed offline using ImageJ. For the intensity profiles of the spot, a line profile was taken for each spot. To measure the signal-to-noise ratio, dark images were subtracted from the spot images and the mean of the intensity of the pixels for each spot was calculated. Signal-to-noise ratio of the spot was obtained by dividing the mean gray value of the foci with the mean gray value of the background region in the corresponding image. The relative percent difference of the background for multiple foci compared with one spot was obtained by measuring the gray value of a background region of an image with the dark image subtracted and then calculating its relative percent difference with the background of the image of one spot, such that, $\frac{B_n - B_{1spot}}{B_{1spot}} \cdot 100\%$, wherein B_n is the background for images with n, number of spots and B_{1spot} is the background of the image with 1 spot. The power of each foci was modulated using the laser diode controller. Power measurements at the sample plane were performed using a power meter (Spectra-Physics, 843-R optical power meter) with a thermopile detector (Spectra Physics, 919P-003-10). The intensity for each spot was calculated by dividing the measured power with the area of the spot, wherein the diameter is given by the full width at half maximum of the spot. The maximum available intensity provided by the setup is 10.7 μW/μm² for single foci and decreases as a function of number of foci.

2.5 | Data analysis

Image stacks of the calcium fluorescence signals were analyzed offline using a custom ImageJ macro and Matlab (MathWorks) scripts. Five cells in the field of view surrounding the photostimulated cell were manually traced. The mean gray value of each cell region with corresponding background subtracted F_i was obtained and recorded for each frame, i. Calcium transients were represented as $\Delta F/F_0$, where F_0 is the basal fluorescence at frame 1. The peak $\Delta F/F_0$ is defined using the following relation, $\frac{\Delta F}{F_0} = \frac{F_i - F_0}{F_0}$.

2.6 | Confocal microsopy

Confocal images were acquired using a confocal microscope (LEICA, TCS, SP5) with Leica Application Suite Advanced Fluorescence software. HL1-ChR2 cells were

prepared as described in sample preparation. Cells were fixed with 4% paraformaldehyde (Carl-Roth) for 30 min at room temperature and then washed afterwards three times with DPBS. The fluorescence image of the membrane-bound yellow fluorescent protein in HL1 cells expressing channelrhodopsin-2 (Figure 1C) was obtained using ×20 objective, NA. 0.5 (LEICA, HCPL Fluor AR). The image was taken using an Argon-ion laser operated at a wavelength of 514 nm with a power of 140 μW measured at the sample plane. The wavelength range detected by the photomultiplier tube is between 528 and 630 nm.

3 | RESULTS

3.1 | Calculation of computer-generated holograms

Central to the control and shaping of light using the FSLM is the calculation of computer-generated holograms (CGH) to be displayed on the FSLM. In our setup detailed in Section 2.1, CGH were displayed on FSLM to focus light on the sample and maximize light efficiency. Expressed in coordinates x and y of the modulator, the phase distribution φ of the Fresnel zone plate used for focusing is

$$\varphi = \frac{\pi \cdot (x^2 + y^2)}{f\lambda}, \tag{1}$$

where f is the focal length of the zone plate and λ is the laser wavelength. Due to the discrete nature of the FSLM, the minimum achievable focal length $f_{\min}$ that maintains maximum efficiency is determined by the pixel pitch Δ and the number of pixels N on the short axis of the modulator:

$$f_{\min} = \frac{N \cdot \Delta^2}{\lambda}. \tag{2}$$

To calculate the CGH, each illuminated point in the sample plane is the result of a Fresnel zone plate in the FSLM plane focusing the light to this point. A computer-generated complex hologram $H(x,y)$ on the SLM can therefore be expressed as the sum of all such Fresnel zone planes, which, in a more compact form, is the convolution of a distribution $M(\tau, \nu)$ in the sample plane containing the relative gray values of all illuminated spots on the sample with a Fresnel zone plate,

$$H(x,y) = \int\int M(x-\tau, y-\nu) \cdot e^{i \cdot \varphi(\tau,\nu)} d\tau d\nu. \tag{3}$$

The Fresnel zone plate can be precalculated for higher computational efficiency. This procedure can be easily be extended to 3-dimensional holograms if two-dimensional holograms are calculated for different sample planes and added after convolution. Since the FSLM used here is a binary phase modulator, complex holograms will have to be converted to binary phase-only holograms. For sparse light distribution of the sample, that is, a combination of single far-apart foci, this can be done by omitting amplitude information from the complex hologram and perform so-called thresholding of the phase:

$$\varphi' = \begin{cases} \pi, & \pi/2 \le \phi < 3\pi/2 \\ 0, & \text{else} \end{cases}. \tag{4}$$

More complex holograms, that is, ones containing uniformly illuminated areas, greatly suffer in quality from thresholding, so bidirectional error diffusion (BERD) [28,33] is implemented to overcome this problem. This method processes all pixels consecutively. Differences between the current pixel value and the desired pixel value are distributed to neighboring unvisited pixels. To avoid artifacts accumulating on one side of the processed images, a meandering bi-directional pattern is used. Figure 2 shows a simulated reconstruction of a hologram resulting in an intensity distribution consisting of 8 foci arranged in a ring pattern. Figure 2A shows the foci reconstructed from a hologram binarized using BERD and the corresponding central part of this hologram is shown in Figure 2C. In comparison, the respective intensity distribution and the central part of a hologram binarized with thresholding can be seen in Figure 2B,D, respectively. Based on the intensity distributions, BERD results in more evenly distributed intensities compared with thresholding. This is further shown by the overlay of normalized cross-section of the individual foci from the 8 foci pattern shown in Figure 2E. Here, the intensity cross-sections reconstructed from holograms binarized with BERD and thresholding are shown in blue and red, respectively. With a mean intensity value of $\overline{y_{\max}} = 0.94 \pm 0.06$, foci generated with BERD are brighter and more consistent than those created by the thresholding which has a mean intensity of $\overline{y_{\max}} = 0.6 \pm 0.13$.

Arbitrary patterns can also be also generated using the binary phase holograms. Figure 3 shows a simulated illumination pattern shaped as a cross with arms 300 μm long and 60 μm wide. Figure 3A,C show the reconstructed image and central part of the hologram using BERD while Figure 3B,D show the respective
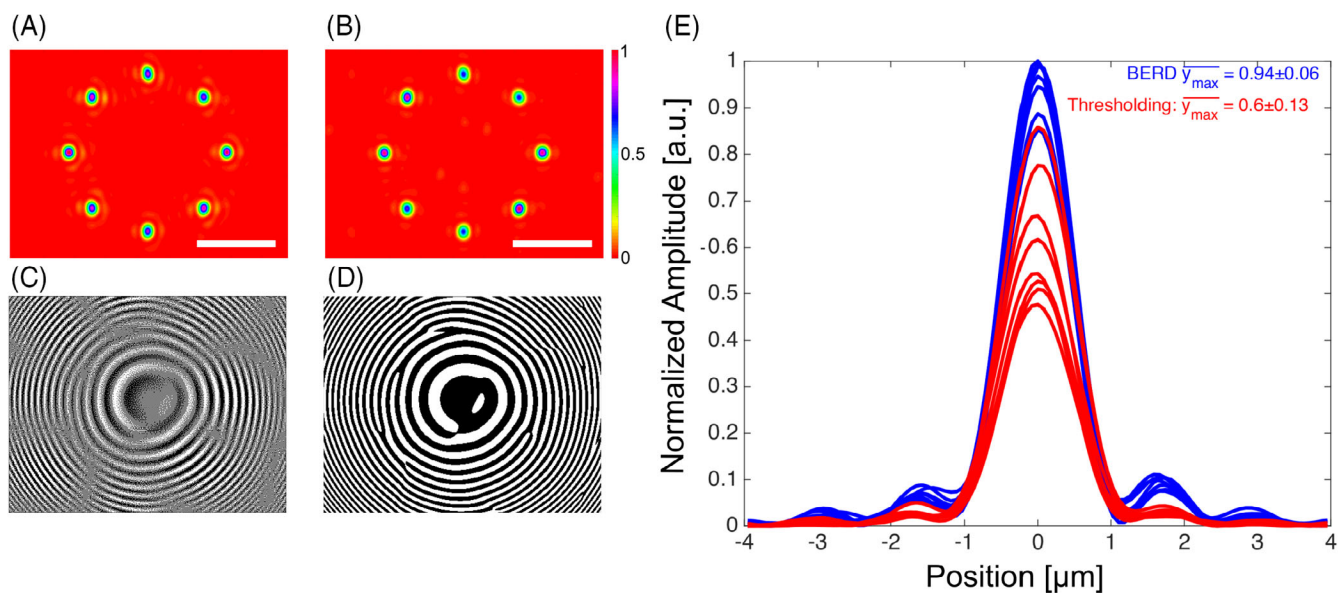
FIGURE 2 Comparison of BERD and thresholding for a simulated pattern consisting of eight points located on a ring. Intensity distributions in false colors reconstructed from holograms binarized using (A) BERD and (B) thresholding. Central part of the corresponding hologram binarized with (C) BERD and (D) thresholding, respectively. (E) Overlay of single spot profiles along the vertical image axis normalized to maximum gray value in both (A) and (B). BERD results in brighter and more even intensity distributions
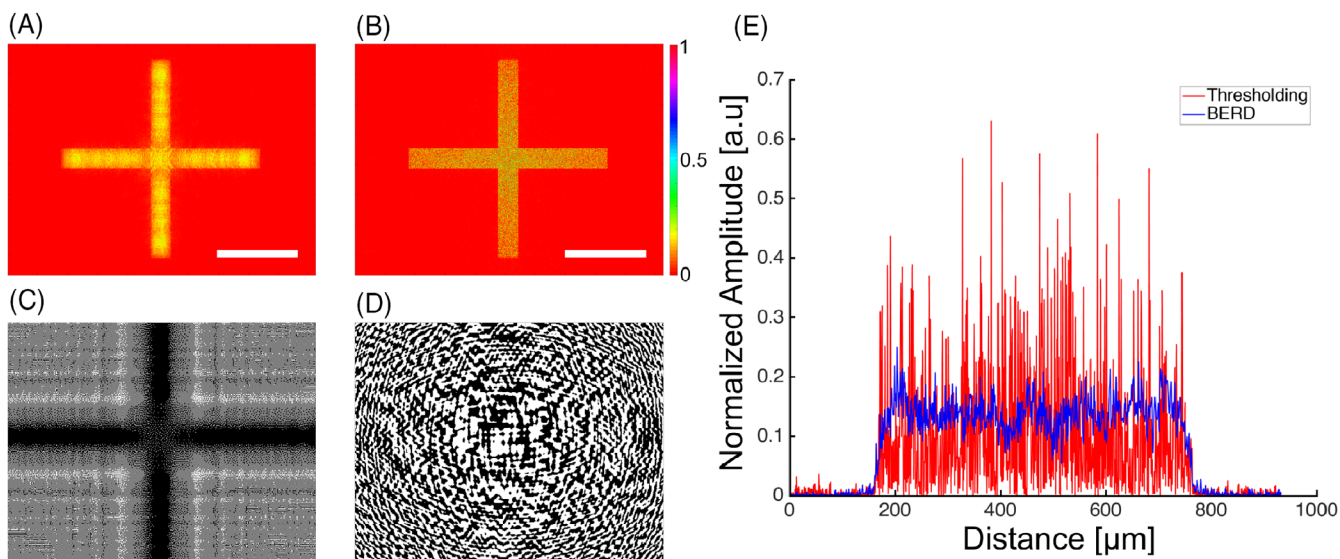

FIGURE 3 Comparison of BERD and thresholding for a simulated pattern consisting a cross with 300 μm long arms. Intensity distribution in false colors reconstructed from holograms binarized using (A) BERD and (B) thresholding. Central part of the corresponding hologram binarized with (C) BERD and (D) thresholding. (E) Horizontal cross-section along the center of the cross. It is clear that using BERD, the patterned light is much less prone to speckles and more evenly distributed, which is important for a consistent stimulation of cells in the illuminated area

images using thresholding. In Figure 3E, we plotted the horizontal cross-section along the center of the cross for the two approaches. By binarizing the holograms using BERD, the intensity distribution is less contaminated by speckles and more uniform, which is important for a

consistent and precise stimulation of cells in the illuminated area.

The flexibility of optogenetic stimulation using FSLM stems from the ease of updating the patterns of foci on the sample. The number, position and

FIGURE 4 (A) Images of generated foci by the SLM (1, 2, 4 and 8 foci). Scale bar is 20 μm. (B) Intensity profile of individual spot (gray trace) and the mean intensity (solid black trace) with increasing number of foci. Note the changes in y-axis for 2, 4 and 8 foci. (C) Measured average FWHM of the foci as a function of number of foci. Error bars represent standard deviation. (D) Intensity of the focused spot with respect to background noise ratio as a function of number of foci generated. Error bars represent standard deviation of the mean gray value of the foci. (E) Relative percent change of the background of the images for 2 or more foci compared with 1 spot
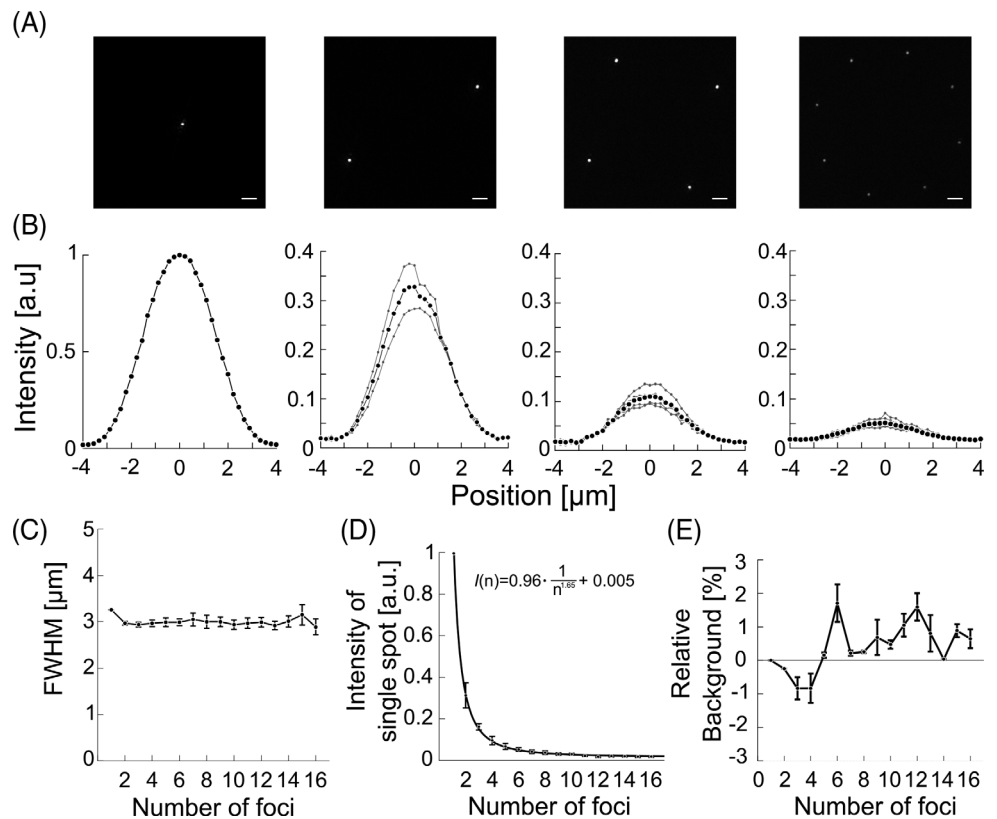

arrangement of the foci can be controlled by simply changing the displayed hologram on the FSLM. The foci could be arranged arbitrarily in any position and arrangement as specified by the user. Furthermore, by precalculating the holograms, the holograms could be stored in the FSLM and updated with the speed depending on the refresh rate of the FSLM. Hence, the number and arrangement of the foci can be dynamically changed during a series of fluorescence acquisition. As we have shown in this section, hologram binarization using BERD is superior to the simpler method of phase thresholding and therefore exclusively used for hologram generation throughout the presented optogenetics experiments.

3.2 | Characterization of generated laser foci using calculated laser generated holograms

We characterized the foci generated by the FSLM for 1 to 16 foci. Figure 4A shows representative images of 1, 2, 4 and 8 foci taken at a fixed camera exposure time and laser power. With increasing number of foci, the intensity of each spot decreases, while the Gaussian intensity profile and the full width at half maximum (FWHM) of each

spot remains the same (Figure 4B). The measured FWHM of each spot is 3.00 ± 0.15 μm which remains constant with increasing number of spots generated as shown in Figure 4C. Figure 4D shows the intensity of the spots as a function of the number of foci generated. The intensity of each single spot is proportional to $n^{-1.65}$, where n indicates the number of foci used. The slight nonlinear dependence of the spot intensity on the number of foci could be attributed to combined effects of the limited spatial frequency of the SLM and the conversion of the complex-valued Fresnel holograms into a binary phase hologram. Additionally, measurement artifacts could be present due to slight non-uniformity of the collected signal depending on the position of the light with respect to the camera sensor. Since any diffused light background can reduce the threshold energy needed to excite the light-sensitive cardiomyocytes, we assessed if the background changes with increasing number of foci. This was determined by measuring the background of the images for different number of foci. We found negligible changes in image background when switching from single to multiple spots as shown in Figure 4E. Relative percent differences of the background for multiple foci compared with 1 spot are on average <2%. This indicates that most of the light at the sample is confined in the laser foci and that no spurious
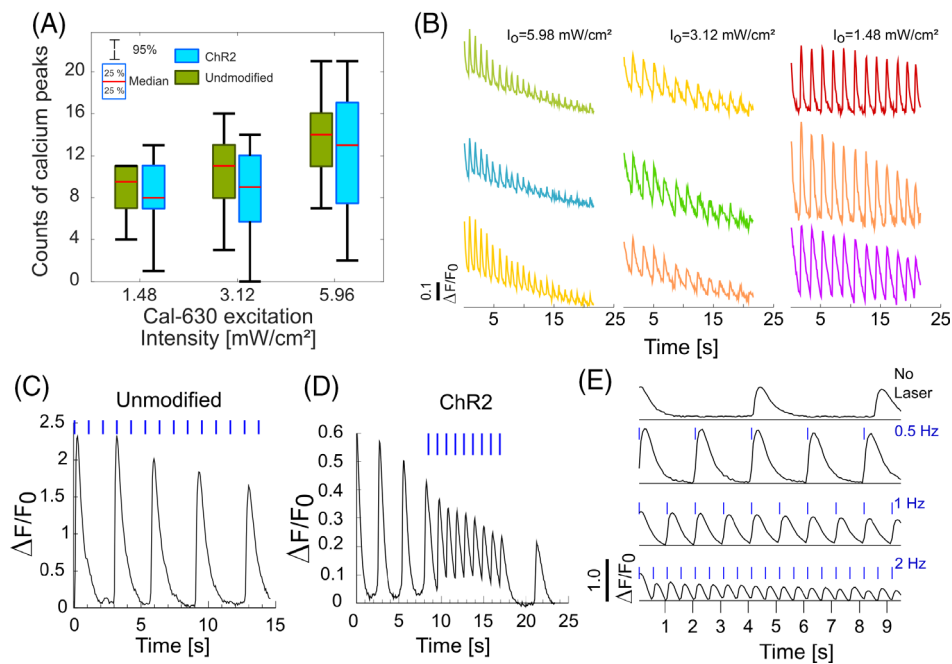
FIGURE 5 (A) Number of spontaneous calcium peaks for HL1-ChR2 cells and unmodified HL1 cells imaged at varying Cal-630 excitation light intensity. (B) Spontaneous calcium traces of HL1-ChR2 cells for different Cal-630 excitation light intensities. The photobleaching rate is fastest for highest Cal-630 excitation light intensity, 5.98 mW/cm². (C) Calcium traces of unmodified HL1 cell illuminated with a laser spot ($I_{spot} = 10.7$ μW/μm², $t_{pulse} = 10$ ms). (D) Calcium transients observed in a photostimulated ChR2 expressing HL1 cell. The cell responds rapidly with each applied laser illumination. (E) Calcium traces for a HL1-ChR2 cell paced at different photostimulation frequencies (0.5, 1 and 2 Hz)

diffused light background should affect the spatial selectivity of the spot excitation.

To measure the accuracy and precision of the positioning of the foci on the sample with the FSLM system, a calibration procedure was implemented where CGHs were precalculated for a set of coordinates corresponding to 40 points on the sample plane as seen in the camera. The system then generates the foci at these points and the positions of the foci were recorded. Based on these positions, coordinate transformation using a 2D second order polynomial fit was performed to correct for any discrepancies. For 10 experiments, the positioning errors obtained in x and y coordinates at the sample plane were $d_x = 0.1 \pm 1.8$ μm and $d_y = 1.2 \pm 1.9$ μm.

3.3 | Evaluation of Cal-630 for calcium imaging and its compatibility for ChR2 photostimulation

To evaluate the compatibility of the commercially available dye, Cal-630 as an optical readout for calcium imaging, unmodified HL1 and HL1-ChR2 cells were stained with this dye and imaged with varying Cal-630 excitation light intensity. HL1 cells are known to express voltage-gated calcium ion channels [34] and therefore exhibit

spontaneous action potentials [35]. During cardiac excitation-contraction coupling, Ca^{2+} in the cytosol increases leading to the opening of voltage-gated calcium ion channels, influx of Ca^{2+} and subsequent release of Ca^{2+} from sarcoplasmic reticulum resulting to contraction [36]. Therefore, cardiac action potential is accompanied by rapid increase in cytosolic Ca^{2+} which can be visualized by calcium imaging. If the light spectral bandwidth (598–613 nm) to excite Cal-630 also photoactivates ChR2, we expect that the continuous illumination of the Cal-630 excitation light will clamp the membrane potential of the cells to a depolarization state and will completely suppress or reduce occurrences of spontaneous action potential [37]. Hence, to confirm that Cal-630 can be used to visualize action potential during optogenetic stimulation with minimal cross-talk, we compared the number of spontaneous calcium peaks for unmodified HL1 cells and HL1-ChR2 cells. Figure 5A shows the number of observed spontaneous calcium peaks for both cell lines. For different intensities of Cal-630 excitation light (I_o), the number of spontaneous calcium peaks are not statistically different between unmodified HL1 and HL1-ChR2 cells (t test, $p > 0.05$). Changes in photobleaching rate were observed for HL1-ChR2 calcium transients which has a faster decay rate with higher Cal-630 excitation light intensity as shown in Figure 5B.
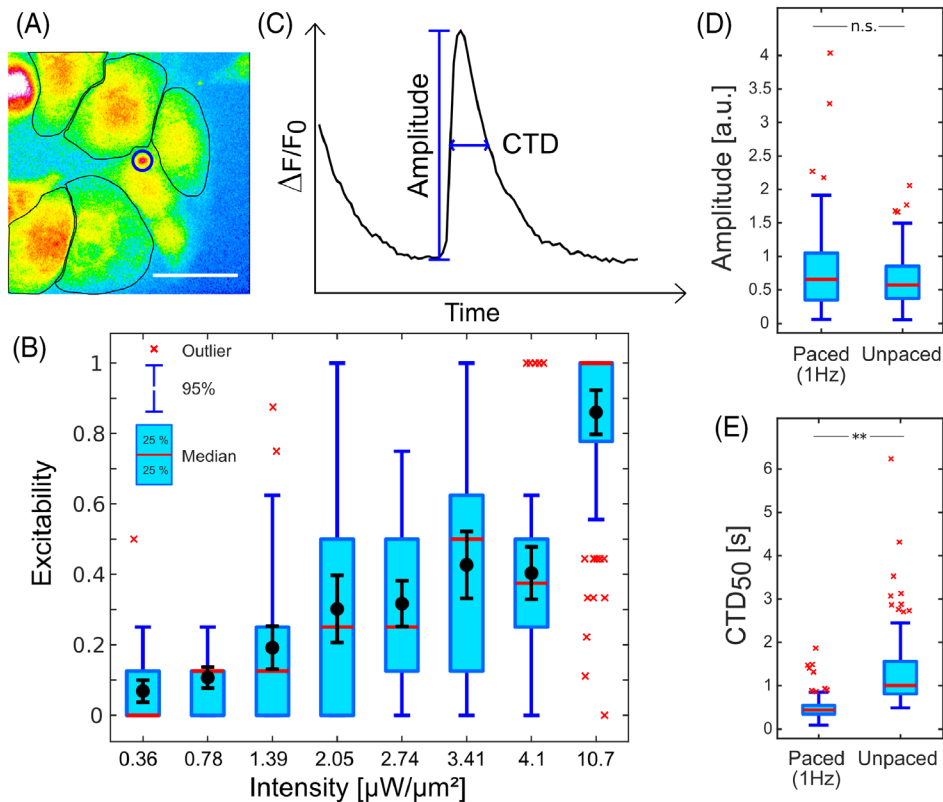
FIGURE 6 (A) A representative fluorescence image of a photostimulated cell and the corresponding cells evaluated for their excitability. The circle depicts the location of the laser on one of the cells in the field of view. Outlined cells were evaluated for their response to the photostimulation. Scale bar is 20 μm. (B) Box plot representation of the excitability of the cells as a function of photostimulation intensity for 1 Hz pacing frequency. Black circles and their error bars are the mean excitability and the standard error of mean for three dishes, respectively. (C) Schematic of the calcium trace indicating the amplitude and the calcium transient duration (CTD). (D) Box plot of the amplitude of the calcium transients and (E) CTD at 50% of the peak measured for paced and spontaneous calcium transients. Statistical significance was tested using unpaired Student's t-test, not significant (ns), $^{**}p < 0.01$

We further confirmed that the blue light photostimulation (pulse duration $t_{pulse} = 10$ ms, $I_{spot} = 10.7$ μW/μm^2) does not elicit calcium transient response on unmodified HL1 cells and any calcium transient activity from HL1-ChR2 are due to the photostimulation of ChR2. As shown in Figure 5C, the calcium transients observed from unmodified HL1 cells occur independently from blue light stimulation. In contrast, calcium transients observed from HL1-ChR2 cells can be modulated with the presence of blue laser spot as shown in Figure 5D. Calcium transients rise rapidly after each photostimulation pulse and the cells' calcium activity return to their spontaneous activity after the blue laser spot was switched off. We observed that the photostimulated HL1-ChR2 cells act as a pacemaker to electrically coupled neighboring cells within the field of view and their electrical activity can be paced with the single micron-sized laser spot. Furthermore, single spot stimulation at this intensity shows efficient light pacing and ChR2-expressing cardiomyocytes can be paced reliably from 0.5 up to 2 Hz as shown in Figure 5E.

3.4 | Excitability of electrically-coupled cardiomyocytes as a function of a single spot photostimulation intensity

To determine the excitability of the cardiac syncytium as a function of laser intensity, we photostimulated a single HL1 cell using a generated laser spot with the holographic system and evaluated the excitability of the neighboring cells. Figure 6A depicts this experiment. A cell in the middle of the field of view was photostimulated and surrounding five cells were individually evaluated for each photostimulation intensity by obtaining the ratio of the number of calcium peaks to the number of photostimulation pulses applied. Experiments were performed on three dishes and five regions per dish were evaluated for each intensity. We calculated the mean value for all the cells evaluated in all samples. Figure 6B shows the dependence of the excitability of the syncytium as a function of laser spot intensity. The excitability increases as a function of the photostimulation intensity. For the lowest intensity $I_{spot} = 0.36$ μW/μm^2,
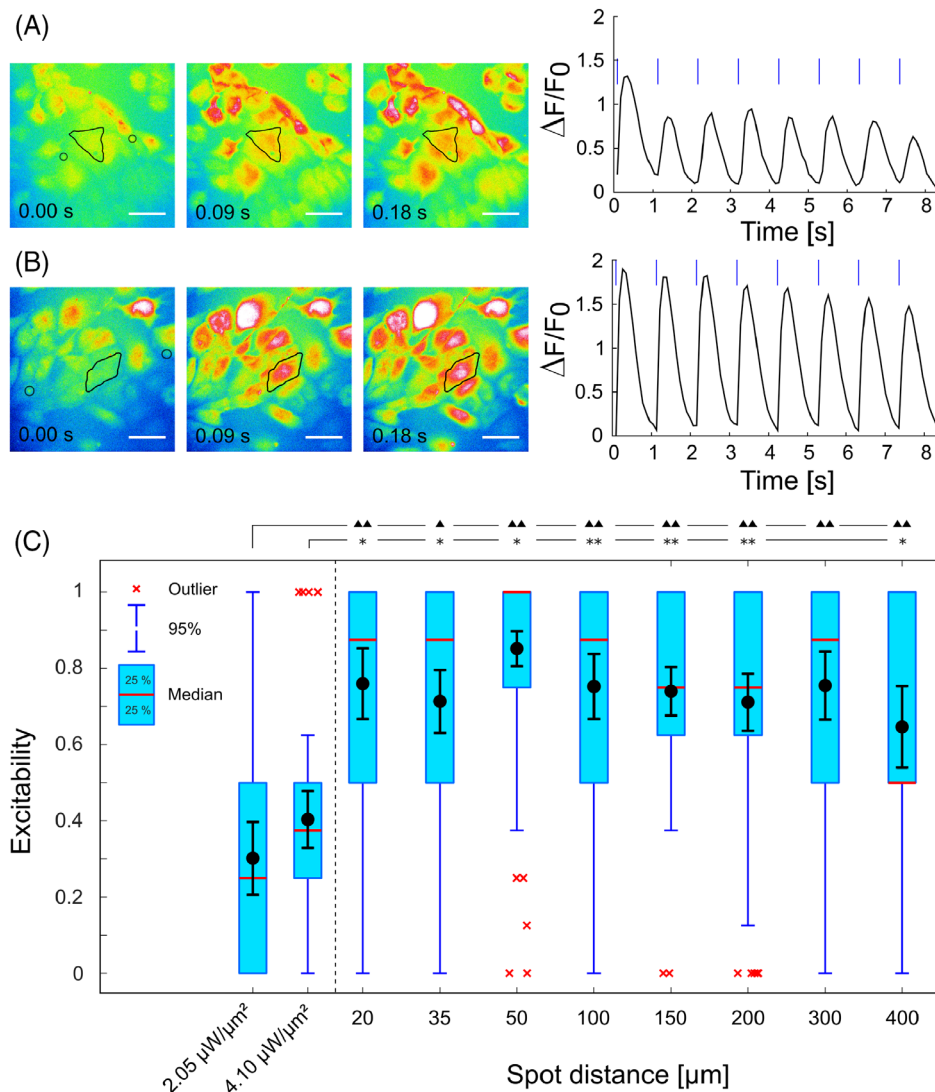
FIGURE 7 (A) Representative image series of photostimulated cells using two holographically generated foci with gap distances of 100 μm and (B) 200 μm. Laser spot locations are marked with circles in left images. Plots show the corresponding calcium traces for the cells marked in the middle. Scale bars are 50 μm. (C) Box plot of the excitability using single and dual spot excitation ($I_{perspot} = 2.05$ μW/μm^2) as a function of spot distance. Black circles and the corresponding error bars are the average of excitability and the standard error of means, respectively ($n = 3$–4 dishes). No statistically significant difference was found between the excitability obtained at different spot distances ($p > 0.5$, one-way ANOVA). Unpaired Student's t-test was used as statistical test to compare the means of the dual spot to single spot stimulation. Symbols *, ▲ correspond to $p < 0.05$ whereas **, ▲▲ to $p < 0.01$

the mean excitability (black circles) is ∼7%, indicating that the intensity of the photostimulation spot is not sufficient to pace the cardiomyocytes and that any calcium transients observed are due to their spontaneous electrical activity. Using higher laser intensities, the excitability increases to 43% ($I_{spot} = 3.4$ μW/μm^2) and 86% ($I_{spot} = 10.7$ μW/μm^2), respectively.

Furthermore, we quantified the amplitude of the calcium peaks as well as the calcium transient duration (CTD) (full width of half maximum of the calcium signal) as schematically described in Figure 6C for the calcium traces of light-paced and spontaneous transients of HL1-ChR2 cells. No significant difference (unpaired Student's t test, $p > 0.05$) was observed between the mean amplitude for paced cells at 1 Hz photostimulation frequency (0.76 ± 0.53 $\Delta F/F_0$), compared with spontaneous calcium transients (0.55 ± 0.30 $\Delta F/F_0$) (Figure 6D). CTDs for paced cells are on average shorter at 0.46 ± 0.19 s compared with spontaneous transients at 1.28 ± 0.79 s

(Figure 6E). This shows that the applied single photostimulation spot has no significant effect on the calcium amplitude but can alter the CTD of the HL1-ChR2 cells. Furthermore, these changes in calcium transient properties can be reported by Cal-630, demonstrating its suitability to quantify the calcium response of cardiomyocytes during optogenetic stimulation.

The holographic setup can also be used to arbitrarily target any optogenetic cell in a functional syncytium, trigger light pacing and initiate electrical conduction from this location. A single spot was generated and directed with the FSLM to the leftmost cell in the field of view. By detecting the calcium trace on the electrically coupled cells from the photostimulated cell, we can estimate the conduction velocity for the region. Figure S1A shows an image wherein the conduction of electrical activity occurs from a single, photostimulated cell to a distal cell of about 200 μm away from the site of the irradiation. The calcium traces of the evaluated cells 1–7 are depicted in Figure S1B

where the calcium rise is delayed the further it is from the laser spot. From these calcium traces, the conduction velocity can be estimated for this particular region to be approximately 0.6 mm/s, slower than conduction velocity of HL1 cells reported in literature [38]. However, we also observed that conduction velocities can highly vary depending on the confluency of the cells.

3.5 | Enhanced excitability with dual spot excitation

We then explored the potential of the holographic system for parallel, dual spot photostimulation. In this scenario, both photostimulated cells will act as efficient pacemakers to electrically coupled cells for high intensities as observed in our single spot photostimulation experiments. Furthermore, within a cardiac syncytium, these pacemakers will be sources of propagating electrical wavefronts via connecting gap junctions between cells. To be able to observe any significant effects in excitability due to the dual spot photostimulation protocol, we opted to use photostimulation parameters which yielded suboptimal excitability (I_{spot} = 2.05 µW/µm^2 and t_{pulse} = 10 ms). By evaluating the excitability of the cells between the two photostimulated cells at varying gaps between the spots, we can also determine if these changes in excitability are spot distance dependent and also interpret how these changes in excitability might be related to wavelength of the propagating electrical wavefronts from the two photocurrent sources.

Representative time series images of cells stimulated using dual spot stimulation are shown for 100 µm (Figure 7A) and 200 µm (Figure 7B) spot distances. In both cases, the calcium traces show that the evaluated cells in the middle of the spots exhibit 1:1 excitability with the applied photostimulation pulse. Other cells in the field of view also showed paced calcium transients in response to the two photostimulated cells. Therefore, dual spot stimulation with the mentioned photostimulation parameters can also pace cells at these spot distances.

We summarize the excitability for single and dual spot stimulation in Figure 7C. Single spot stimulation with laser intensity of 2.05 µW/µm^2 exhibited <50% mean excitability. However, with dual spot stimulation, the excitability was enhanced to 85 ± 5% (50 µm distance, 2.05 µW/µm^2 per spot). We tested the statistical difference between single spot, I_{spot} = 2.05 µW/µm^2 and dual spot for all gap distances using unpaired Student's t test to determine if this enhancement in excitability is significant. The excitability values obtained for all gap distances were statistically different from single spot,

I_{spot} = 2.05 µW/µm^2 as indicated by ▲ ($p < 0.05$) and ▲▲ ($p < 0.01$) in Figure 7C. The enhanced excitability persisted up to spot distance of 300 µm (75 ± 9%) and only slightly decreased when changing the distance between the spots to 400 µm (63 ± 11%) although this change is not statistically significant. The mean excitability for each spot distance did not correspond to a significant statistical change as tested using one-way ANOVA. For distances further than 400 µm, the spots will be significantly outside our field of view and would be difficult to ensure that cells are illuminated by the spots.

We also compared the excitability values obtained using dual spot stimulation to a single spot with intensity of 4.10 µW/µm^2 corresponding to the cumulative intensity of the dual spots. Using single spot, I_{spot} = 4.10 µW/µm^2, the excitability of the cells were 40 ± 7%. Except for gap distance of 300 µm, the excitability values for dual spot stimulation were still statistically different from the values obtained using single spot, I_{spot} = 4.10 µW/µm^2 as indicated by * ($p < 0.05$) and ** ($p < 0.01$). Overall, our experiments show that dual spot stimulation enhances the excitability of the optogenetic cells even for spot distances up to 400 µm.

4 | DISCUSSION

Optogenetics represents a powerful tool for pacing and inhibition towards new understanding of electrophysiology in a functional syncytium. In this study, a holographic-based optogenetic setup with an optical readout was designed and built for parallel and flexible targeting of single cells expressing ChR2. The binary phase ferroelectric SLM and driver used in this study require the preparation and upload of holograms prior to the experiments but can achieve 100x faster refresh rate than the traditional liquid crystal SLMs. Other available driver versions of FSLM allow for online control of the displayed holograms at lower refresh rates around several hundred frames per second and would require a more complicated software interfaced with OpenGL by Psychtoolbox or comparable software. In comparison, acousto-optical deflectors can be operated at MHz switching rates [16] but cannot truly simultaneously stimulate several cells. Liquid crystal SLMs have slower switching rates but projection of multiple holographic spots generated by this SLM can also be time-gated with DMDs for faster rate of selective switching of light patterns [39]. In most optogenetic applications especially in cardiac systems, DMDs have been used for binary amplitude modulation [18–20,37,40–42]. However, for focusing inside the biological tissue using techniques such as

digital phase conjugation or adaptive optics, ferroelectric SLMs exhibit twice higher signal to background noise ratio compared with binary amplitude-based DMDs [25,43]. For applications, such as stimulation beyond the epicardial layers, this would be extremely useful especially in a strongly scattering cardiac tissue. Future configurations could also include using holographic fiber-endoscopy [44] in a catheter format to be inserted into a heart chamber for targeted optogenetic stimulation [45]. We find that for the Fresnel holograms used in our setup, binarization using BERD is superior to phase thresholding. Previous study using FSLMs used random superposition and phase thresholding for hologram generation [26] is not readily comparable to our study since it used Fourier holograms which cannot be binarized easily without a random phase distribution in the sample plane.

As an optical readout, chemical calcium indicators have been shown to robustly detect changes in intracellular calcium in cardiomyocytes. In optogenetic stimulation, brief photostimulation induces contraction by a sequence of events. Photostimulation of ChR2 leads to instantaneous depolarization and opening of voltage-gated Ca^{2+} channels followed by transmembrane inflow of Ca^{2+} leading to Ca^{2+} release from the sarcoplasmic reticulum stores and subsequently resulting in a global wave of Ca^{2+} [46]. Hence, calcium imaging have been shown to be a sufficient alternative readout to membrane potential imaging [47]. As a chemical calcium dye, Cal-630′s absorption is well separated from ChR2 absorption which makes it a spectrally compatible indicator to detect ChR2 excitation. Calcium chemical dyes such as Rhod-4, ($\lambda_{exc}/\lambda_{em}$ = 523 nm/551 nm) [48] and CaSiR-1 ($\lambda_{exc}/\lambda_{em}$ = 620 nm/664 nm) [49] have both been reported for crosstalk-free optical detection while stimulating ChR2 and its variants [50,51]. One drawback of certain calcium dyes compared with genetically encoded calcium indicators is the sequestration of the signals to subcellular organelles as reported by others [52]. Within the duration of our experiments, typically around 30 min, we did not observe compartmentalization of the Cal 630 dye within the intracellular organelles. In comparison, voltage imaging imposes stringent requirements in the imaging system (e.g., intense light sources and sensitive camera) since any emission only comes from the plasma membrane where the voltage-sensitive dye is localized to be able to properly report membrane voltage changes [53,54]. Nonetheless, with state-of-the-art voltage-sensitive dyes, several groups have reported successful membrane voltage imaging combined with optogenetics using dyes such as BeRST1 [55], Pittsburg-I (PGH1) [33] and the ANNEPS-based red-shifted versions di-4-ANBDQBS [50] and di-4-

ANBDQPQ [11,18,19]. As shown in our study, Cal-630 provides low background and large fluorescence change in response to intracellular calcium changes in cardiac cells upon photostimulation. Modest photobleaching was observed in our experiments which we found to be largely dependent on the intensity of the imaging light used. Thus, Cal-630 is an excellent optical read-out for ChR2 optogenetic stimulation.

Few pacemaker cells control the regular beating of the heart. In a cardiac network, electrotonic interactions occur which allow the spread of action potential from a few pacemaker cells to neighboring cardiomyocytes. It is hypothesized that gap junctions mediate the conduction of electrical activity such that action potential can be rapidly transmitted throughout the syncytium [56]. HL1 cells are known to express connexins 40, 43, 45 which are abundant in gap junctions [38]. In this study, the activity of a cardiac network was investigated in response to a single localized spot stimulation. Despite the rather small laser spot size, 3 µm FWHM, surrounding non-illuminated cells within a 200 µm region are excited which indicates action potential coupling with the photostimulated HL1-ChR2 cells. However, we also observe some cells stained with calcium dye in each region which are unresponsive to light stimulation. This could indicate heterogeneity in the cardiac properties of the HL1 cells [38] as well as in the expression level of ChR2 in the individual cells.

The ability of the system to arbitrarily position stimulation at any location allows us to test different protocols to probe cell to cell coupling interactions in the syncytium. Based on the excitability measurements we obtained for single spot excitation, the intensities of 2 and 4 µW/µm^2 have an excitability of <50%. But exciting a cardiac network with dual spot compared with single spot stimulation resulted in a marked enhancement in mean excitability. We reasoned that if the two photocurrent sources act independently, then the excitability would remain unchanged compared with single spot stimulation. However, if electrotonic conduction due to sub-threshold changes in membrane potential induced by the dual spots have occurred, we would expect that at a certain range of spot distances, a decay in excitability would be observed due to photocurrent source-sink mismatch [56,57]. We observed though that increased excitability persisted even up to distances of 400 µm. Although excitability decreased from 75% to 62.5% at 400 µm, the gap between the foci is not sufficient to completely abolish the enhanced excitability. We initially considered the possibility that increase in diffused background light could have occurred when dual spots are generated. In this scenario, the increase in excitability of

the cardiac network with dual spot stimulation could be explained by reduction of the spot excitation threshold needed to efficiently pace the cardiac cells. However, the relative change in diffused background light for two foci compared with single spot has been negligible as shown in our measurements. To further understand the mechanism behind this enhancement, future studies will involve imaging the electrical activity at larger field of view to observe excitability at larger spot distances during parallel stimulation.

A limitation of our study is that we did not fully capitalized on the speed of the FSLM. However, we expect that our system could have potential applications in probing the dynamics of electrical wavefronts in other cardiac systems which have faster electrical wavefront dynamics. For such experiments, a larger field of view would be recommended for optical mapping of the wavefronts in the cardiac monolayer. It has been proposed that with an optogenetic cardiac system, one can use this approach to design protocols to treat arrhythmia [58]. Burton et al. have demonstrated that optogenetics can be used to control chirality of macroscopic spiral waves using patterned light [20]. Studies using parallel light actuation combined with imaging have contributed to our understanding in designing effective strategies to effectively extinguish fibrillation in abnormal cardiac models [37]. Conduction blocks using patterned light to defibrillate whole mouse hearts [18] or in ChR2 expressing cardiomyocyte monolayers [41,42] show promise in using novel light patterns for low-energy defibrillation. Precise spatio-temporal control of the light foci as demonstrated in our study can also be introduced in the path of the electrical wavefronts to perturb, initiate or block spiral waves in a syncytium in diseased and normal cardiac cell models.

5 | CONCLUSION

This study demonstrates an all-optical ferroelectric SLM holographic-based system for optogenetic stimulation and imaging of optical read-out in a cardiac syncytium. We show that calcium imaging with Cal-630 enables robust imaging of calcium transients during optogenetic stimulation. Localized holographic single spot stimulation using a fast ferroelectric SLM is sufficient to trigger cardiac action potentials in a group of cells. The universal control and shaping of light permits us to create multiple origins of activation which increased the excitability of the syncytium compared with single spot stimulation. Overall, our study shows the potential of an all-optical optogenetic system in quantifying cardiac electrophysiology of a functional syncytium.

DATA AVAILABILITY STATEMENT

Matlab scripts for creation and displaying binary phase holograms on ferroelectric binary phase modulators can be found in the following link DOI: 10.5281/zenodo. 6281875.

ORCID

Felix Schmieder https://orcid.org/0000-0003-0799-1743
Maria Leilani Torres-Mapa https://orcid.org/0000-0003-2761-9586

REFERENCES

[1] P. Sasse, *Circ. Arrhythm. Electrophysiol.* **2011**, *4*(5), 598.
[2] P. Sasse, M. Funken, T. Beiert, T. Bruegmann, *Front. Physiol.* **2019**, *10*, 675.
[3] H. G. Mond, A. Proclemerer, *Pacing Clin. Electrophysiol.* **2011**, *8*, 34.
[4] S. K. Mulpuru, M. Madhavan, C. J. McLeod, Y. M. Cha, P. A. Friedman, *J. Am. Coll. Cardiol.* **2017** jan, *69*(2), 189.
[5] T. Bruegmann, D. Malan, M. Hesse, T. Beiert, C. J. Fuegemann, B. K. Fleischmann, P. Sasse, *Nat. Methods* **2010**, *7*(11), 897.
[6] U. Nussinovitch, L. Gepstein, *Nat. Biotechnol.* **2015**, *33*(7), 750.
[7] T. Bruegmann, P. M. Boyle, C. C. Vogt, T. V. Karathanos, H. J. Arevalo, B. K. Fleischmann, N. A. Trayanova, P. Sasse, *J. Clin. Investig.* **2016**, *126*(10), 3894.
[8] T. Bruegmann, T. Beiert, C. C. Vogt, J. W. Schrickel, P. Sasse, *Cardiovasc. Res.* **2018** apr, *114*(5), 713.
[9] M. Funken, D. Malan, P. Sasse, T. Bruegmann, *Front. Physiol.* **2019** apr, *10*(APR), e498.
[10] T. Zaglia, N. Pianca, G. Borile, F. da Broi, C. Richter, M. Campione, et al., *Proc. Natl. Acad. Sci.* **2015**, *112*(32), E4495.
[11] R. A. Quiñonez Uribe, S. Luther, L. Diaz-Maue, C. Richter, *Front. Physiol.* **2018**, *9*, e1651.
[12] J. P. Rickgauer, D. W. Tank, *Proc. Natl. Acad. Sci.* **2009**, *106*(35), 15025.
[13] L. Carrillo-Reid, W. Yang, Y. Bando, D. S. Peterka, R. Yuste, *Science* **2016**, *353*(6300), 691.
[14] L. Carrillo-Reid, S. Han, W. Yang, A. Akrouh, R. Yuste, *Cell* **2019**, *178*(2), 447.
[15] R. Prakash, O. Yizhar, B. Grewe, C. Ramakrishnan, N. Wang, I. Goshen, A. M. Packer, D. S. Peterka, R. Yuste, M. J. Schnitzer, K. Deisseroth, *Nat. Methods* **2012**, *9*(12), 1171.

[16] O. Hernandez, K. Pietrajtis, B. Mathieu, S. Dieudonné, *Sci. Rep.* **2018**, *8*(1), 13768.

[17] E. Ronzitti, C. Ventalon, M. Canepari, B. C. Forget, E. Papagiakoumou, V. Emiliani, *J Opt* **2017**, *19*(11), 113001.

[18] C. Crocini, C. Ferrantini, R. Coppini, M. Scardigli, P. Yan, L. M. Loew, G. Smith, E. Cerbai, C. Poggesi, F. S. Pavone, L. Sacconi, *Sci. Rep.* **2016**, *6*(1), 35628.

[19] M. Scardigli, C. Müllenbroich, E. Margoni, S. Cannazzaro, C. Crocini, C. Ferrantini, R. Coppini, P. Yan, L. M. Loew, M. Campione, L. Bocchi, D. Giulietti, E. Cerbai, C. Poggesi, G. Bub, F. S. Pavone, L. Sacconi, *J. Physiol.* **2018**, *596*(17), 3841.

[20] R. A. B. Burton, A. Klimas, C. M. Ambrosi, J. Tomek, A. Corbett, E. Entcheva, G. Bub, *Nat Photon* **2015**, *9*(12), 813.

[21] S. Turtaev, I. T. Leite, K. J. Mitchell, M. J. Padgett, D. B. Phillips, T. Čižmár, *Opt. Express* **2017**, *25*(24), 29874.

[22] E. Papagiakoumou, F. Anselmi, A. Bègue, V. de Sars, J. Glückstad, E. Y. Isacoff, V. Emiliani, *Nat. Methods* **2010**, *7*(10), 848.

[23] A. M. Packer, L. E. Russell, H. W. P. Dalgleish, M. Häusser, *Nat. Methods* **2015** feb, *12*(2), 140.

[24] M. dal Maschio, J. C. Donovan, T. O. Helmbrecht, H. Baier, *Neuron* **2017**, *94*(4), 774.

[25] I. M. Vellekoop, *Opt. Express* **2015** may, *23*(9), 12189.

[26] I. Reutsky-Gefen, L. Golan, N. Farah, A. Schejter, L. Tsur, I. Brosh, S. Shoham, *Nat Commun* **2013**, *4*(1), 1509.

[27] F. Schmieder, S. Klapper, N. Koukourakis, V. Busskamp, J. Czarske, *Appl Sci* **2018**, *8*(7), 1180.

[28] P. W. M. Tsang, T. C. Poon, *Opt. Express* **2013**, *21*(20), 23680.

[29] J. Y. Lin, M. Z. Lin, P. Steinbach, R. Y. Tsien, *Biophys. J.* **2009**, *3*, 96.

[30] Spectrum [Cal-630] | AAT Bioquest. https://www.aatbio.com/fluorescence-excitation-emission-spectrum-graph-viewer/cal_630, **2021**.

[31] Laborbedarf, optische Filter und Lichtquellen | AHF analysentechnik AG. https://www.ahf.de/, **2021**.

[32] N. N. Agladze, O. V. Halaidych, V. A. Tsvelaya, T. Bruegmann, C. Kilgus, P. Sasse, K. I. Agladze, *Biomater. Sci.* **2017**, *5*(9), 1777.

[33] S. A. Park, S. R. Lee, L. Tung, D. T. Yue, *Sci. Rep.* **2015**, *4*(1), 6125.

[34] M. Xia, *J. Mol. Cell. Cardiol.* **2004** jan, *36*(1), 111.

[35] Z. Yang, K. T. Murray, *J. Cardiovasc. Pharmacol.* **2011**, *57*(1), 28.

[36] J. Hüser, L. A. Blatter, S. L. Lipsius, *J. Physiol.* **2000**, *4*(524), 415.

[37] A. Gruber, O. Edri, I. Huber, G. Arbel, A. Gepstein, A. Shiti, N. Shaheen, S. Chorna, M. Landesberg, L. Gepstein, *JCI Insight* **2021**, *6*(11), e147470.

[38] P. Dias, T. Desplantez, M. A. El-Harasis, R. A. Chowdhury, N. D. Ullrich, A. Cabestrero de Diego, et al., *PLoS One* **2014**, *9*(2), e90266.

[39] M. A. Go, M. S. To, C. Stricker, S. Redman, H. A. Bachor, G. J. Stuart, V. R. Daria, *Front. Cell. Neurosci.* **2013**, *7*, e231.

[40] A. B. Arrenberg, D. Y. R. Stainier, H. Baier, J. Huisken, *Science* **2010**, *330*(6006), 971.

[41] I. Feola, L. Volkers, R. Majumder, A. Teplenin, M. J. Schalij, A. V. Panfilov, A. A. F. De Vries, D. A. Pijnappels, *Circ. Arrhythm. Electrophysiol.* **2017**, *10*(11), e005591.

[42] R. Majumder, I. Feola, A. S. Teplenin, A. A. de Vries, A. V. Panfilov, D. A. Pijnappels, *Elife* **2018**, *7*.

[43] Y. Liu, C. Ma, Y. Shen, J. Shi, L. V. Wang, *Optica* **2017**, *4*(2), 280.

[44] R. Kuschmierz, E. Scharf, N. Koukourakis, J. W. Czarske, *Opt. Lett.* **2018**, *43*(12), 2997.

[45] A. Klimas, E. Entcheva, *J. Biomed. Opt.* **2014**, *19*(8), 080701.

[46] E. A. Ferenczi, X. Tan, C. L. H. Huang, *Front. Physiol.* **2019**, *10*, e1096.

[47] C. Houston, K. N. Tzortzis, C. Roney, A. Saglietto, D. S. Pitcher, C. D. Cantwell, R. A. Chowdhury, F. S. Ng, N. S. Peters, E. Dupont, *J. Mol. Cell. Cardiol.* **2018**, *119*, 155.

[48] M. Oheim, M. van't Hoff, A. Feltz, A. Zamaleeva, J. M. Mallet, M. Collot, *Biochim Biophys Acta: Mol Cell Res.* **2014** oct, *1843*(10), 2284.

[49] T. Egawa, K. Hanaoka, Y. Koide, S. Ujita, N. Takahashi, Y. Ikegaya, N. Matsuki, T. Terai, T. Ueno, T. Komatsu, T. Nagano, *J. Am. Chem. Soc.* **2011**, *133*(36), 14157.

[50] A. Klimas, C. M. Ambrosi, J. Yu, J. C. Williams, H. Bien, E. Entcheva, *Nat Commun* **2016**, *7*(1), 11542.

[51] N. S. Soor, P. Quicke, C. L. Howe, K. T. Pang, M. A. A. Neil, S. R. Schultz, A. J. Foust, *J. Phys. D Appl. Phys.* **2019** mar, *52*(10), 104002.

[52] T. J. Collins, P. Lipp, M. J. Berridge, M. D. Bootman, *J. Biol. Chem.* **2001**, *7*(276), 26411.

[53] R. U. Kulkarni, E. W. Miller, *Biochemistry* **2017**, *10*(56), 5171.

[54] Y. Bando, C. Grimm, V. H. Cornejo, R. Yuste, *BMC Biol.* **2019**, *12*(17), 71.

[55] A. Klimas, G. Oritz, S. C. Boggess, E. W. Miller, E. Entcheva, *Prog. Biophys. Mol. Biol.* **2020**, *8*(154), 62.

[56] S. Dhein, T. Seidel, A. Salameh, J. Jozwiak, A. Hagen, M. Kostelka, G. Hindricks, FW. Mohr, *Front. Physiol.* **2014**, *5*, 424.

[57] Y. Xie, D. Sato, A. Garfinkel, Z. Qu, J. N. Weiss, *Biophys. J.* **2010**, *99*(5), 1408.

[58] E. Entcheva, G. Bub, *J. Physiol.* **2016**, *594*(9), 2503.

SUPPORTING INFORMATION

Additional supporting information may be found in the online version of the article at the publisher's website.